



**HAL**  
open science

# Experimental investigation of formation and decomposition of roaldite in ammonia atmosphere at 300–700 °C and associated nitrogen isotope fractionations

Long Li, Pierre Cartigny, Kan Li

► **To cite this version:**

Long Li, Pierre Cartigny, Kan Li. Experimental investigation of formation and decomposition of roaldite in ammonia atmosphere at 300–700 °C and associated nitrogen isotope fractionations. *Geochimica et Cosmochimica Acta*, 2021, 300, pp.65-78. 10.1016/j.gca.2021.02.033 . hal-03236244

**HAL Id: hal-03236244**

**<https://u-paris.hal.science/hal-03236244>**

Submitted on 15 Mar 2023

**HAL** is a multi-disciplinary open access archive for the deposit and dissemination of scientific research documents, whether they are published or not. The documents may come from teaching and research institutions in France or abroad, or from public or private research centers.

L'archive ouverte pluridisciplinaire **HAL**, est destinée au dépôt et à la diffusion de documents scientifiques de niveau recherche, publiés ou non, émanant des établissements d'enseignement et de recherche français ou étrangers, des laboratoires publics ou privés.



Distributed under a Creative Commons Attribution - NonCommercial 4.0 International License



13

## Abstract

14           Roaldite ( $\text{Fe}_4\text{N}$ ) is one of the few nitride minerals found in meteorites. Their nitrogen (N)  
15 isotopic signatures carry important information for understanding the early N cycle in the proto-  
16 solar nebula. However, the lack of knowledge on the N isotopic effects from nitride formation to  
17 its survival from frictional heating during landing impedes the interpretation and application of N  
18 isotope compositions of nitride minerals in meteorites. Here, we carried out laboratory  
19 experiments under a recently proposed roaldite forming condition, i.e.,  $\text{NH}_3$  (as starting N  
20 source) reacting with metallic Fe at medium temperatures. We observed  $\text{Fe}_4\text{N}$  formation over a  
21 large range of temperatures from 300 °C to 700 °C. The formation of  $\text{Fe}_4\text{N}$  was associated with  
22 equilibrium N isotope fractionations with  $\alpha_{\text{Fe}_4\text{N-NH}_3}$  values of 0.9907 ( $\pm 0.0004$ ) at 300 °C and  
23 0.9936 ( $\pm 0.0004$ ) at 500 °C, respectively. In the experimental pressure conditions (initial  $P_{\text{NH}_3} =$   
24 3.9-6.4 bar,  $P_{\text{Total}} < 8.3$  bar), the formed  $\text{Fe}_4\text{N}$  remained stable at 300 °C, but was unstable and  
25 quickly decomposed to Fe and  $\text{N}_2$  at 500 °C and 700 °C. The decomposition of  $\text{Fe}_4\text{N}$  was  
26 associated with large kinetic isotope fractionations with  $\alpha_{\text{N}_2-\text{Fe}_4\text{N}}$  values of 0.9811 ( $\pm 0.0009$ ) at  
27 500 °C and 0.9839 ( $\pm 0.0011$ ) at 700 °C, respectively. Our experimental results suggest that  
28 roaldite formed from  $\text{NH}_3$  can carry an isotopic signature very close to that of its source, but  
29 partial decomposition (if there is any) can easily shift its N isotope composition for several tens  
30 of per mil, and in extreme cases, to  $> 300\%$ . Thus, great caution is needed when using N isotope  
31 composition of roaldite (and probably other nitride minerals as well) to trace source information.

## 32 **1. Introduction**

33 Nitride minerals, such as carlsbergite (CrN; Buchwald and Scott, 1971), roaldite (Fe<sub>4</sub>N;  
34 Buchwald and Nielsen, 1981), osbornite (TiN; Bannister, 1941; Keil, 1969), sinoite (Si<sub>2</sub>N<sub>2</sub>O;  
35 Andersen et al., 1964), nierite (Si<sub>3</sub>N<sub>4</sub>; Leitner et al., 2018), and uakitite (VN; Sharygin et al.,  
36 2018), have been discovered in a variety of meteorite samples. These nitride minerals, together  
37 with ammonium salts (Poch et al., 2020) and organic compounds (Pizzarello et al., 2011),  
38 represent the few major nitrogen (N) carriers in meteorites and other solar material; their N  
39 isotope compositions (expressed as either <sup>14</sup>N/<sup>15</sup>N ratio or the delta notation  $\delta^{15}\text{N} =$   
40  $(^{15}\text{N}/^{14}\text{N})_{\text{sample}} / (^{15}\text{N}/^{14}\text{N})_{\text{Air}} - 1$ ) have been used to infer the isotopic signatures of N reservoirs in  
41 the solar system (e.g., Prombo and Clayton, 1993; Pizzarello et al., 1994; Meibom et al., 2007;  
42 Ponganis and Marti, 2007; Füri and Marty, 2015; Grewal et al., 2021). In addition, since enstatite  
43 chondrites likely contributed to a majority of the building blocks of the Earth (Javoy et al., 2010;  
44 Dauphas, 2017; Piani et al., 2020), the nitride in enstatite chondrite (e.g., Rubin and Choi, 2009;  
45 Leitner et al., 2018) could have at least partially contributed to Earth's primary N reservoir, and  
46 consequently affected the N geochemical and isotope compositions of Earth's reservoirs (Javoy,  
47 1998; Marty, 2012).

48 Isotopic studies on nitride minerals in meteorites yielded a huge range of N isotope  
49 compositions. For example, a number of studies on iron meteorites and pallasites obtained  
50 variable  $\delta^{15}\text{N}$  values from -96‰ to 164‰ for these meteorites (Meibom et al., 2007; Grewal et  
51 al., 2021 and references therein); Meibom et al. (2007) observed  $\delta^{15}\text{N}$  values around -360‰ for  
52 osbornite in CAI from the carbonaceous chondrite Isheyevo; whereas Harries et al. (2015)  
53 observed  $\delta^{15}\text{N}$  values from 44‰ to 64‰ for carlsbergite in the volatile-rich CM2 chondrites  
54 Yamato 791198 and Y-793321. To fully interpret these isotopic data, it is crucial to assess the N

55 isotopic effects over the course from the formation of nitride minerals in their source regions to  
56 their final landing/emplacement on Earth's surface, which however has not been taken into  
57 account in most previous studies due to the lack of N isotope fractionation data.

58         Recently, through laboratory experiments, Li et al. (2016) and Dalou et al. (2019)  
59 investigated the N isotope fractionations between silicate melt and metal alloys. These  
60 experiments yielded very different isotope fractionation factors, but consistently showed strong  
61 <sup>15</sup>N-depletion in metal alloys. This mechanism may provide insights into the interpretation of N  
62 isotope compositions of nitrides in differentiated planetary bodies, such as iron meteorites, but  
63 may not be relevant to nitride minerals in primitive chondrites which have not undergone  
64 significant silicate-metal differentiation. Through study of mineral inclusions in primitive  
65 chondritic meteorites, Harries et al. (2015) suggested that the nitride mineral (carlsbergite in this  
66 case) was likely formed by reaction between (Cr-bearing) metal with ammonia gas at  
67 temperatures slightly higher than 300-400 °C.

68         To examine the formation and stability of nitride at medium temperatures and determine  
69 the associated N isotope fractionations, we carried out laboratory experiments to study the  
70 reaction between metallic Fe powders and NH<sub>3</sub> gas at 300-700 °C. This temperature range spans  
71 over the proposed formation temperature of the carlsbergite-bearing sulfide in CM2 chondrite  
72 (Harries et al., 2015) and also can be applicable to early Earth's near surface hydrothermal  
73 systems. Iron nitride (rather than chromium nitride) was chosen for this study because, as an  
74 initial effort to study the metal-NH<sub>3</sub> system, the reaction between NH<sub>3</sub> and Fe can be better  
75 constrained and is easier to accomplish in laboratory conditions.

76

## 77 **2. Experiment setup and analytical methods**

78           The experimental setup and analytical method employed in this study were similar to  
79 those in a previous experimental study on the N isotope fractionations of thermal decomposition  
80 of NH<sub>3</sub> without the presence of Fe (Li et al., 2009). But some of the experimental conditions  
81 (e.g., temperature, reagents) have been modified for the purpose of this study.

82           In brief, about 20 mg commercial metallic iron (Fe) powders (VWR; purity > 99.5%)  
83 were loaded into a one-end sealed, pre-cleaned (by combustion under air at 1200 °C for 2 hours)  
84 quartz tube (outer diameter: 6 mm; inner diameter: 4 mm). For comparison, ~ 50 mg and ~ 6 mg  
85 Fe powders were also used in the 500 °C experiments. The sample tube was then attached to a  
86 glass vacuum line illustrated in Li et al. (2009) to remove air. An aliquot of NH<sub>3</sub> gas (with initial  
87  $\delta^{15}\text{N}$  value of -2.2‰; n = 10;  $1\sigma = 0.1\%$ ) was expanded from a large-volume NH<sub>3</sub> gas flask and  
88 equilibrated for 2 minutes (to ensure pressure and isotopic homogenization) before it was  
89 cryogenically transferred into the sample tube. The method for NH<sub>3</sub> quantification has been  
90 described in detail by Li et al. (2009) and not reiterated here. After minor incondensable gases  
91 were evacuated, the sample tube was sealed under vacuum, and carefully measured for its inner  
92 length to allow the estimation of internal pressure.

93           A number of sample tubes (for parallel experiments) were put into a muffle furnace and  
94 carefully positioned to minimize the thermal gradient along and between the tubes. The  
95 experiments were proceeded at 300 °C for 28 to 244 hours, 500 °C for 10 minutes to 168 hours,  
96 and 700 °C for 2-15 minutes. Temperature monitoring indicates that temperature overshooting  
97 only occurred in the 700 °C experiments because a rapid heating ramp was programed to  
98 minimize the time to reach peak temperature. But the magnitude of temperature overshooting

99 was small ( $< 5\text{ }^{\circ}\text{C}$ ) and lasted for a short time (a few seconds). The sample tubes were then  
100 quenched, loaded into tube crackers attached to the same vacuum line, pumped, and cracked. The  
101 released gases, including  $\text{H}_2$ ,  $\text{N}_2$ , and remaining  $\text{NH}_3$ , were quantified in sequence using a  
102 Toepler pump.  $\text{N}_2$  and  $\text{NH}_3$  were also measured for N isotope compositions using an isotope ratio  
103 mass spectrometer at dual-inlet mode, all described in detail by Li et al. (2009).

104 The solid phases of selected samples from each temperature were investigated by X-ray  
105 diffraction (XRD) and scanning electron microscope (SEM) to identify the mineral phases and  
106 morphology. The solid phases of ten samples from the  $500\text{ }^{\circ}\text{C}$  experiments were also loaded into  
107 one end-sealed quartz tubes together with  $\sim 1\text{g}$  CuO oxidant, pumped, sealed under vacuum, and  
108 combusted at  $1000\text{ }^{\circ}\text{C}$  overnight in a muffle furnace to release any N for quantification and  
109 isotopic analysis. As control experiments, the remaining solid phases of some of these samples  
110 after the measurements were again loaded into quartz tubes with CuO oxidant, evacuated, sealed  
111 and combusted at  $1000\text{ }^{\circ}\text{C}$  by the same procedure. No N was yielded in these control  
112 experiments, indicating that metallic Fe could not re-assimilate  $\text{N}_2$  during the cooling of the  
113 sample tubes, likely due to the preferential oxidation by  $\text{O}_2$  released from CuO.

114 Based on repeated analyses of international standards IAEA-N1 and IAEA-N2 over the  
115 course of these experiments, the analytical uncertainty was generally  $< 2\%$  ( $1\sigma$ ) of the absolute  
116 value for N quantity, and  $< 0.15\text{‰}$  ( $1\sigma$ ) for N isotope composition. The variation of plateau  
117 temperature of the muffle furnace during the experiments was  $\pm 1\text{ }^{\circ}\text{C}$ .

118

### 119 **3. Results**

120 The quantities and isotope compositions of the reactants and products of all the  
121 experiments with their temperature and pressure conditions are listed in Table 1.

122 At each experimental temperature,  $\text{NH}_3$  decreased steadily with progressive  $^{15}\text{N}$   
123 enrichment in the remaining  $\text{NH}_3$  along experimental time (Figs. 1, 2A).  $\text{N}_2$  was also detected in  
124 the gaseous phases in all experiments (Fig. 1). While the produced  $\text{N}_2$  also display progressively  
125 larger yields and higher  $\delta^{15}\text{N}$  values along experimental time, the  $\delta^{15}\text{N}_{\text{N}_2}$  values are all lower  
126 than the  $\delta^{15}\text{N}$  values of the initial  $\text{NH}_3$  (Fig. 2B). This general pattern is similar to the  
127 experimental results of thermal decomposition of  $\text{NH}_3$  in the absence of Fe (Li et al., 2009),  
128 suggesting that  $\text{NH}_3$  decomposition and  $\text{N}_2$  production occurred in the experiments in this study.

129 The decomposition rates of  $\text{NH}_3$  in the experiments in this study were mainly controlled  
130 by two factors. One is the amount of Fe. For example, under the same condition of 500 °C and 1  
131 hour, the experiments using ~6 mg, ~20 mg, ~50 mg Fe yielded 60% ( $1\sigma = 2\%$ ;  $n=2$ ), 43% ( $1\sigma$   
132 = 1%;  $n = 4$ ), and 40% ( $1\sigma = 1\%$ ;  $n = 2$ ) remaining  $\text{NH}_3$ , respectively (Table 1; Fig. 3). The  
133 other and the main controlling factor is temperature. For example, in the 300 °C experiments,  
134 ~80% of initial  $\text{NH}_3$  still remained after 10 days; in the 500°C experiments, ~40% of initial  $\text{NH}_3$   
135 remained after 1 hour; in the 700°C experiments, only 7%  $\text{NH}_3$  was left after 15 minutes (Table  
136 1), and no  $\text{NH}_3$  was detected after 30 minutes. For comparison, Li et al. (2009) showed that, in  
137 similar experimental conditions but with the absence of Fe,  $\text{NH}_3$  decomposition at 700 °C  
138 occurred at a much slower rate (e.g., ~75% remained after 40 hours and ~40% remained after 10  
139 days) and even no decomposition could be detected over months at temperature  $\leq 500$  °C. This  
140 comparison indicates that Fe can accelerate the  $\text{NH}_3$  decomposition reaction for orders of  
141 magnitude and can expand the reaction to much lower temperatures ( $\leq 300$  °C).

142 In contrast to the experiments by Li et al. (2009), which showed good matches in both  
143 nitrogen mass and isotope composition between decomposed NH<sub>3</sub> and produced N<sub>2</sub>, the  
144 experiments in this study gave obvious mismatches between these two. For example, in the 300  
145 °C experiments, NH<sub>3</sub> was the major N-bearing species observed in the remaining gas phases after  
146 28 hours and 244 hours, but only accounts for ~80% of initial NH<sub>3</sub> (Fig. 1A); nearly 20% of NH<sub>3</sub>  
147 was consumed with little production of N<sub>2</sub> but significant production of H<sub>2</sub> (Table 1). This leads  
148 to significant amounts of “missing” N. In the 500 °C and 700 °C experiments, more N<sub>2</sub> occurred  
149 together with NH<sub>3</sub> in the remaining gas phases (Fig. 1B & C). But again the total amounts of N  
150 recovered from NH<sub>3</sub> and N<sub>2</sub> are less than that of the initial NH<sub>3</sub> in the relatively short  
151 experiments, leading to various amounts of “missing” N (Table 1).

152 This “missing” N has been recovered by the combustion of the solid phases. For example,  
153 in the 500 °C experiments, the mass balance of the quantities and isotope compositions of the  
154 recovered NH<sub>3</sub> and N<sub>2</sub> in the gases phases and the recovered N from the solid phases gave a total  
155 N yield (relative to the initial NH<sub>3</sub>) of 96.7% with a δ<sup>15</sup>N value of -1.9‰ from one of the 10  
156 minute experiments, 98.3% (1σ = 0.1%; n = 3) with a mean δ<sup>15</sup>N value of -2.3‰ (1σ = 0.1‰; n  
157 = 3) from three of the 1 hour experiments, 98.5% (1σ = 1.0%; n = 3) with a mean δ<sup>15</sup>N value of -  
158 2.1‰ (1σ = 0.4%; n = 3) from three of the 2 hour experiments, 102.6% with a δ<sup>15</sup>N value of -  
159 2.8‰ from one of the 3.5 hour experiments, and 99.5% (1σ = 0.4%; n = 2) with a mean δ<sup>15</sup>N  
160 value of -3.1‰ (1σ = 0.0‰; n = 2) from two of the 6 hour experiments (Table 1; Fig. 1B & E).  
161 These δ<sup>15</sup>N values match well with the δ<sup>15</sup>N value (-2.2‰) of the initial NH<sub>3</sub>.

162 H<sub>2</sub> was also examined in some of the experiments. Measurements from a number of  
163 experiments (n = 2, 15 and 3 for the 300°C, 500°C and 700°C experiments, respectively) indicate  
164 that the molar ratio between the H of recovered H<sub>2</sub> and the N of decomposed NH<sub>3</sub> (hereafter

165 referred to as the H:N ratio) is strongly dependent on experimental duration (Fig. 4). The highest  
166 H:N ratios (2.8-2.9) observed in the shortest experiments (10 minutes at 500 °C and 700 °C) are  
167 close to the H:N stoichiometric ratio of 3 in NH<sub>3</sub>, which verifies that the H<sub>2</sub> was produced from  
168 the decomposition of NH<sub>3</sub>. The H:N ratios progressively decrease along experimental time to as  
169 low as ~2.2 in the longest experiment of 244 hours at 300 °C (Table 1; Fig. 4). Because hydrogen  
170 solubility in Fe at the experimental temperatures is extremely low ( $N_H/N_{Fe} < 10^{-4}$ ; Kiuchi and  
171 McLellan, 1983), it cannot account for any detectable decrease in the H:N ratio. The slightly  
172 lowered H:N ratios (by 0.1-0.2) in the short experiments were likely caused by quick oxidation  
173 of H<sub>2</sub> by small amounts of Fe oxides on the surface of the Fe reactant or some small oxidizing  
174 particles attached on the inner wall of the quartz tubes; whereas the progressively decreasing  
175 H:N ratios in long experiments were likely caused by diffusive loss of H<sub>2</sub> out of the quartz tubes  
176 (Li et al., 2009). Nevertheless, the reasonably good match between the decomposed NH<sub>3</sub> and  
177 recovered H<sub>2</sub> in the short experiments suggests that no H-bearing phase was formed in the solid  
178 phases and all H in the decomposed NH<sub>3</sub> was released as H<sub>2</sub> in the gas phases.

179

## 180 **4. Discussion**

### 181 **4.1. Formation and stability of Fe<sub>4</sub>N**

182 To further understand the form of the fixed N in metallic Fe, we examined the solid phases  
183 by XRD and SEM. The XRD spectra (Fig. 4) clearly show that an Fe-nitride phase, Fe<sub>4</sub>N, has  
184 been formed in the Fe particles at all temperatures. Although thermodynamic models predicted  
185 that other nitride phases such as Fe<sub>2-3</sub>N could also be formed and co-exist with Fe<sub>4</sub>N in the high-  
186 nitriding potential NH<sub>3</sub> atmosphere (e.g., van Voorthuysen et al., 2002; Pelka et al., 2009), we  
187 did not detect these nitride phases in any of our experiments (Fig. 5). This may be attributed

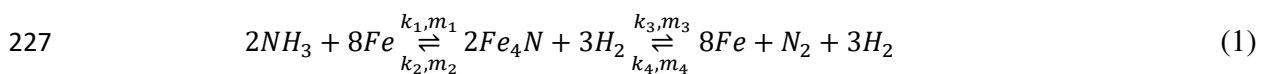
188 either to the relatively short experimental durations which were not long enough to form  $\text{Fe}_{2-3}\text{N}$   
189 or to the decreased nitriding potential as a result of decreased  $\text{NH}_3$  partial pressure and increase  
190  $\text{H}_2$  partial pressure with the progress of the experiments (van Voorthuysen et al., 2002; Pelka et  
191 al., 2014). In all the 300 °C and 500 °C experiments (Fig. 5A & B),  $\text{Fe}_4\text{N}$  is the only detectable  
192 nitride phase; whereas in the 700 °C experiments, another Fe nitride phase that can be described  
193 as  $\text{FeN}_{0.088}$  (a tetragonal phase in  $I4/mmm$  space group) was also detected in addition to  $\text{Fe}_4\text{N}$   
194 (Fig. 5C). These results suggest that,  $\text{Fe}_4\text{N}$  is a relatively more stable phase than  $\text{FeN}_{0.088}$  and  
195 other Fe-nitrides in our experimental conditions.

196 Thermodynamically,  $\text{Fe}_4\text{N}$  is unstable at relatively low (e.g., atmospheric)  $\text{N}_2$  pressures  
197 (Ertl et al., 1979; Wriedt et al., 1987). However, the proceeding of  $\text{Fe}_4\text{N}$  decomposition is  
198 believed to be strongly controlled by N desorption from “surface nitride” and followed migration  
199 of N from the depth to the surface in the solid phases, which are only significant above 400-450  
200 °C because of the high kinetic energy required for N desorption from Fe and for recombination  
201 of N atoms to  $\text{N}_2$  (Ertl et al., 1979; van Voorthuysen et al., 2002). These high kinetic barriers  
202 maintain  $\text{Fe}_4\text{N}$  as a metastable phase in the 300 °C experiments (with no sign of decomposition  
203 after more than 10 days). At 500 °C and 700 °C, the energy is high enough to facilitate the  
204 decomposition of  $\text{Fe}_4\text{N}$  (van Voorthuysen et al., 2002). As a result,  $\text{Fe}_4\text{N}$  can only occur for a  
205 short time period at these temperatures and be inevitably decomposed with the consumption of  
206 the limited  $\text{NH}_3$  reservoir.  $\text{Fe}_4\text{N}$  could occur persistently in these high temperature conditions if  
207 an unlimited  $\text{NH}_3$  reservoir exists to maintain the  $\text{NH}_3 - \text{Fe}_4\text{N}$  reaction.

208 The entire process from uptake of N by Fe (to form  $\text{Fe}_4\text{N}$ ) to subsequent decomposition of  
209  $\text{Fe}_4\text{N}$  is clearly illustrated by the SEM images (Fig. 6). Compared with the relatively rough and  
210 random surface features of initial Fe particles (Fig. 6A), the solid phases from the experiment at

211 300 °C for 244 hours display clear growth of nanocrystals on Fe surface (Fig. 6B), which has  
 212 been verified to be Fe<sub>4</sub>N by XRD (Fig. 5A) and EDX-SEM analyses. The growth of Fe<sub>4</sub>N on Fe  
 213 surface was not well ordered but in an indistinct morphology at the early stage (e.g., Fig. 6C, F),  
 214 suggesting that the formation of Fe<sub>4</sub>N on Fe surface occurred very fast. With the further  
 215 processing of the reaction along time, Fe<sub>4</sub>N was reorganized into nanocrystals in an octahedral  
 216 geometry (Fig. 6B, E & G), which is consistent with the structure of Fe<sub>4</sub>N, but different to the  
 217 hexagonal structure of Fe<sub>3</sub>N (Inokuti et al., 1975; Jacobs et al., 1995) or the tetragonal structure  
 218 of FeN<sub>0.088</sub>. Another interesting feature on Fe surface is the annular stepped surface morphology  
 219 (Fig. 6E, G), which may be related to the reorganization of Fe after Fe<sub>4</sub>N decomposition. EDX-  
 220 SEM analysis also detected a small oxygen peak from the initial Fe particles, implying the Fe  
 221 reagent in our experiments contained small amount of oxygen, which could explain the slightly  
 222 lowered H:N ratios in the short experiments (Fig. 4).

223 Based on above observations, our experiments demonstrates that NH<sub>3</sub> decomposition  
 224 occurred through denitridation, which was ultimately destabilized to produce N<sub>2</sub> gas. It can be  
 225 described by at least two sets of reactions between (1) NH<sub>3</sub> and Fe<sub>4</sub>N and (2) Fe<sub>4</sub>N and N<sub>2</sub>. The  
 226 total reaction in the system can be described using a general reaction formula:



228 in which k<sub>1</sub> and k<sub>3</sub> denote the reaction rate constants of the forward reactions and k<sub>2</sub> and k<sub>4</sub>  
 229 denote the reaction rate constants of the inverse reactions; m<sub>1</sub> to m<sub>4</sub> denote the order of  
 230 corresponding reaction.

231 Our 500°C experiments gave the largest number of time-series data from 10 minutes to 168

232 hours (Table 1), which provide a best opportunity to quantitatively model the reactions. Based on  
 233 the comparison of the NH<sub>3</sub> decomposition extents among various Fe quantity (Fig. 3), it appears  
 234 that that 20 mg Fe, which was used in most of the experiments, was in (or at least close to)  
 235 excess for the reactions and thus not rate-limiting. Therefore, in the modeling, the reaction rates  
 236 were assumed to be independent of the Fe amounts.

237 Based on Equation (1), the decomposition rate of NH<sub>3</sub> and the production rates of Fe<sub>4</sub>N and  
 238 N<sub>2</sub> can be written as:

$$239 \quad \frac{dn_{NH_3}}{dt} = -k_1 \cdot n_{NH_3}^{m_1} + k_2 \cdot n_{Fe_4N}^{m_2} \quad (2)$$

$$240 \quad \frac{dn_{Fe_4N}}{dt} = k_1 \cdot n_{NH_3}^{m_1} - k_2 \cdot n_{Fe_4N}^{m_2} - k_3 \cdot n_{Fe_4N}^{m_3} + k_4 \cdot n_{N_2}^{m_4} \quad (3)$$

$$241 \quad \frac{dn_{N_2}}{dt} = k_3 \cdot n_{Fe_4N}^{m_3} - k_4 \cdot n_{N_2}^{m_4} \quad (4)$$

242 Using Equations (2)-(4), we modeled the quantity evolution of NH<sub>3</sub>, Fe<sub>4</sub>N and N<sub>2</sub> along  
 243 experimental time for the 500 °C experiments. The modeling employed a simplified forward  
 244 numeric calculation approach using a time increment of 1 minute and artificially assigned values  
 245 for k<sub>1</sub> to k<sub>4</sub> and m<sub>1</sub> to m<sub>4</sub>. The best fitting curves shown in Fig. 7A capture most of the  
 246 experimental data and more importantly the overall evolution trend, although a perfect match of  
 247 data was not achieved. Possible uncertainties that may account for the discrepancy between the  
 248 experimental and modeling results include (1) reactions in the temperature ramping stage (< 2  
 249 minutes); (2) potential effect of H<sub>2</sub> (and its diffusive loss over time); (3) the partially oxidized  
 250 surface (although very minor) of the initial Fe powders which could have affected NH<sub>3</sub>  
 251 decomposition rate, at least at the beginning before its surface was completely reduced; (4) the

252 grain size/shape of Fe particles, which could affect the interaction between N and Fe (e.g. Pelka  
253 et al., 2009); (5) some other kinetic effects, such as kinetic crystallization, migration of N  
254 between the depth and the reaction surface of Fe. All these factors could play a role but are  
255 difficult to be quantitatively assessed in the modeling.

256 The best fitting of the experimental data (Fig. 7A) yielded 2, 1, and 0.5 for  $m_1$  to  $m_3$ ,  
257 respectively. The value of  $m_4$  does not significantly affect the results. The best fitting also gave  
258  $k_1/k_2 \approx 2.5$ ,  $k_2/k_3 \approx 100$ , and  $k_3/k_4 \approx 100$ . This indicates that  $k_1$  and  $k_2$  are close, and about two  
259 orders of magnitude larger than  $k_3$ ; the latter is another two orders of magnitude larger than  $k_4$ .  
260 The fact that  $k_1$  and  $k_2$  are close strongly suggests that the reaction between  $\text{NH}_3$  and  $\text{Fe}_4\text{N}$  is  
261 relatively fast and reversible, which are consistent with the quick development of a metastable  
262 state of the  $\text{NH}_3 - \text{Fe}_4\text{N}$  system in the 300 °C experiments (Fig. 1A) and the experiments in the  
263 first 2 hours at 500 °C (Figs. 1B & 7).

264 Compared with the  $\text{NH}_3 - \text{Fe}_4\text{N}$  reaction,  $\text{Fe}_4\text{N}$  decomposition proceeded much more  
265 slowly in the experiments. Because the back-reaction (i.e.,  $\text{N}_2$  conversion to  $\text{Fe}_4\text{N}$ ) is two orders  
266 of magnitude slower and thus can be neglected, the  $\text{Fe}_4\text{N}$  decomposition reaction can be  
267 considered as unidirectional and the rate-limiting step in the entire system.

## 268 **4.2. Nitrogen isotope fractionations during formation and decomposition of $\text{Fe}_4\text{N}$**

### 269 **4.2.1. Modeling of nitrogen isotope fractionation factors**

270 In our experiments, the remaining  $\text{NH}_3$  and the produced  $\text{Fe}_4\text{N}$  and  $\text{N}_2$  show large  $\delta^{15}\text{N}$   
271 variations (Figs. 1-2). With the proceeding of  $\text{NH}_3$  decomposition and  $\text{N}_2$  production, both the  
272 remaining  $\text{NH}_3$  and produced  $\text{N}_2$  are progressively more enriched in  $^{15}\text{N}$ . However, compared

273 with the initial NH<sub>3</sub>, all the remaining NH<sub>3</sub> is more <sup>15</sup>N-enriched, whereas all the produced N<sub>2</sub> is  
 274 more <sup>15</sup>N-depleted and only reaches the δ<sup>15</sup>N value of the initial NH<sub>3</sub> when all the initial NH<sub>3</sub> is  
 275 converted into N<sub>2</sub> (Figs. 1 & 3). In contrast, Fe<sub>4</sub>N shows more variable δ<sup>15</sup>N values, which can  
 276 be either lower or higher than that of the initial NH<sub>3</sub> (Table 1; Fig. 1E). This indicates strong  
 277 isotopic effects associated with the NH<sub>3</sub> – Fe<sub>4</sub>N and Fe<sub>4</sub>N – N<sub>2</sub> reactions.

278 To model the isotope fractionation factor, Equations (5) and (6) can be used for  
 279 equilibrium isotope fractionations:

$$280 \quad \alpha_{P-R} = \frac{(\delta_{R0}+1) - (\delta_R+1) \cdot f_R}{(\delta_R+1) \cdot (1-f_R)} \quad (5)$$

$$281 \quad \alpha_{P-R} = \frac{(\delta_P+1) \cdot (1-f_P)}{(\delta_{R0}+1) - (\delta_P+1) \cdot f_P} \quad (6)$$

282 in which α is the fractionation factor, P denotes product, R denotes reactant, f denotes fraction,  
 283 and δ<sub>R0</sub> is the initial isotope composition of the reactant, i.e., NH<sub>3</sub> in this case.

284 Equations (7) and (8) can be used for the modeling of kinetic isotope fractionation:

$$285 \quad \alpha_{P-R} = \frac{\ln\left(f_R \cdot \frac{1+R_{R0}}{1+R_R} \cdot \frac{R_R}{R_{R0}}\right)}{\ln\left(f_R \cdot \frac{1+R_{R0}}{1+R_R}\right)} \quad (7)$$

286 in which R<sub>R0</sub> and R<sub>R0</sub> denote the initial and final isotopic ratio of the reactant, respectively.

287 Replacement of isotopic ratio by δ (= R<sub>R</sub>/R<sub>STD</sub> - 1) value yields:

$$288 \quad \alpha_{P-R} = \frac{\ln\left[f_R \cdot \frac{1+(1+\delta_{R0}) \cdot R_{STD}}{1+(1+\delta_R) \cdot R_{STD}} \cdot \frac{1+\delta_R}{1+\delta_{R0}}\right]}{\ln\left[f_R \cdot \frac{1+(1+\delta_{R0}) \cdot R_{STD}}{1+(1+\delta_R) \cdot R_{STD}}\right]} \quad (8)$$

289 in which R<sub>STD</sub> is the isotopic ratio of standard, i.e., 0.0036765 for the N isotope standard of

290 atmospheric N<sub>2</sub> (Coplen et al., 1992).

291 It is noted that Equations (5)-(8) are derived with no or minimum (and valid)  
292 approximation (Hayes, 2004), and thus are more complicated than the commonly used Rayleigh  
293 or batch fractionation equations derived with approximations. Hayes (2004) and Scott et al.  
294 (2004) have demonstrated that the simplified equations with approximations can introduce large  
295 errors in the calculation of isotope fractionation factors when involve data with f<sub>R</sub> values close to  
296 0 (i.e., the reaction proceeds close to completion), which is the case of some of our experiments.

297 Equations (5)-(8) are effective for the modeling of isotope fractionations in relatively  
298 simple reactions but difficult for complicated system involving multiple simultaneous reactions  
299 with both equilibrium and kinetic isotopic effects. By integrating equilibrium and kinetic isotope  
300 fractionation factors into a group of functions, Li et al. (2021) introduced a more sophisticated  
301 model to account for the nitrogen isotopic pattern in the process of NH<sub>4</sub><sup>+</sup> dissociation into  
302 aqueous ammonia (NH<sub>3</sub>·nH<sub>2</sub>O) followed by ammonia degassing. The NH<sub>4</sub><sup>+</sup> – NH<sub>3</sub>·nH<sub>2</sub>O – NH<sub>3</sub>  
303 system is similar to the NH<sub>3</sub> – Fe<sub>4</sub>N – N<sub>2</sub> system studied here in that the first reaction is  
304 reversible with possible achievement of isotope equilibration, whereas the second reaction is  
305 unidirectional and dominated by kinetic isotopic effect. Following Li et al. (2021), the isotopic  
306 evolution of NH<sub>3</sub>, Fe<sub>4</sub>N and N<sub>2</sub> in the system can be modeled by rewriting Equations (2)-(4) for  
307 <sup>14</sup>N and <sup>15</sup>N, respectively:

$$308 \quad \frac{dn_{(^{14}NH_3)}}{dt} = -^{14}k_1 \cdot n_{(^{14}NH_3)}^{m_1} + ^{14}k_2 \cdot n_{(^{14}Fe_4N)}^{m_2} \quad (9)$$

$$309 \quad \frac{dn_{(^{15}NH_3)}}{dt} = -^{15}k_1 \cdot n_{(^{15}NH_3)}^{m_1} + ^{15}k_2 \cdot n_{(^{15}Fe_4N)}^{m_2} \quad (10)$$

$$310 \quad \frac{dn_{(^{14}\text{Fe}_4\text{N})}}{dt} = {}^{14}k_1 \cdot n_{(^{14}\text{NH}_3)}^{m_1} - {}^{14}k_2 \cdot n_{(^{14}\text{Fe}_4\text{N})}^{m_2} - {}^{14}k_3 \cdot n_{(^{14}\text{Fe}_4\text{N})}^{m_3} + {}^{14}k_4 \cdot n_{(^{14}\text{N}_2)}^{m_4}$$

311 (11)

$$312 \quad \frac{dn_{(^{15}\text{Fe}_4\text{N})}}{dt} = {}^{15}k_1 \cdot n_{(^{15}\text{NH}_3)}^{m_1} - {}^{15}k_2 \cdot n_{(^{15}\text{Fe}_4\text{N})}^{m_2} - {}^{15}k_3 \cdot n_{(^{15}\text{Fe}_4\text{N})}^{m_3} + {}^{15}k_4 \cdot n_{(^{15}\text{N}_2)}^{m_4}$$

313 (12)

$$314 \quad \frac{dn_{(^{14}\text{N}_2)}}{dt} = {}^{14}k_3 \cdot n_{(^{14}\text{Fe}_4\text{N})}^{m_3} - {}^{14}k_4 \cdot n_{(^{14}\text{N}_2)}^{m_4}$$

314 (13)

$$315 \quad \frac{dn_{(^{15}\text{N}_2)}}{dt} = {}^{15}k_3 \cdot n_{(^{15}\text{Fe}_4\text{N})}^{m_3} - {}^{15}k_4 \cdot n_{(^{15}\text{N}_2)}^{m_4}$$

315 (14)

316 in which  ${}^{14}K_1$  to  ${}^{14}K_4$  and  ${}^{15}K_1$  to  ${}^{15}K_4$  denote the reaction rates of  ${}^{14}\text{N}$  and  ${}^{15}\text{N}$  in corresponding  
 317 reactions, respectively. Consequently, the N isotope fractionations for the  $\text{NH}_3 - \text{Fe}_4\text{N}$  reaction  
 318 and the  $\text{Fe}_4\text{N} - \text{N}_2$  reaction can be described as:

$$319 \quad \alpha_{\text{Fe}_4\text{N}-\text{NH}_3} = \frac{{}^{15}k_2 \cdot {}^{14}k_1}{{}^{14}k_2 \cdot {}^{15}k_1}$$

319 (15)

$$320 \quad \alpha_{\text{N}_2-\text{Fe}_4\text{N}} = \frac{{}^{15}k_4 \cdot {}^{14}k_3}{{}^{14}k_4 \cdot {}^{15}k_3}$$

320 (16)

321 This model involves several parameters, such as the equilibrium and kinetic isotope fractionation  
 322 factors and the order of each reaction. If more than 1 of these parameters are unknown, the  
 323 modeling results may give relatively large errors and require a large dataset for the modeling in  
 324 order to minimize the errors.

#### 325 4.2.2. Equilibrium isotope fractionation factors between $\text{Fe}_4\text{N}$ and $\text{NH}_3$

326 The modeling for the 300 °C experiments is relatively simple because only the first step  
327 reaction of NH<sub>3</sub>–Fe<sub>4</sub>N occurred in the system. The modeling yielded a good linear relationship  
328 ( $R^2 = 0.999$ ) using Equation 5 (for equilibrium isotope fractionations; Fig. 8A) but a bad linear  
329 relationship ( $R^2 = 0.24$ ; not shown here) using Equation 8 (for kinetic isotope fractionations).  
330 This is consistent with an equilibrium isotope fractionation dominating the reaction. The slope on  
331 Fig. 8A gave the equilibrium isotope fractionation factor  $\alpha_{\text{Fe}_4\text{N-NH}_3} = 0.9907 \pm 0.0004$ , or  
332  $1000\ln\alpha_{\text{Fe}_4\text{N-NH}_3} = -9.3 \pm 0.4\text{‰}$  at 300 °C.

333 The modeling of equilibrium isotope fractionation factor for 500°C is more challenging  
334 because the Fe<sub>4</sub>N in most of the experiments has decomposed to various extents (Fig. 1B). An  
335 additional isotopic effect associated with Fe<sub>4</sub>N decomposition could have influenced the isotope  
336 composition of the remaining Fe<sub>4</sub>N, which was further passed on to impact the isotope  
337 composition of the remaining NH<sub>3</sub> due to the fast isotopic exchange between NH<sub>3</sub> and Fe<sub>4</sub>N. As  
338 a result, the  $\delta^{15}\text{N}$  values of the remaining NH<sub>3</sub> in the time-series experiments (Fig. 1E) show a  
339 more complicated pattern. Ideally, these experimental data can be modeled by Equations (9)-  
340 (16). However, because the parameters of  $m_1$  to  $m_4$  are not well constrained and the isotope  
341 fractionation factor for Fe<sub>4</sub>N – N<sub>2</sub> at 500 °C is unknown, the modeling is more empirical.  
342 Nevertheless, the best fitting of the large isotopic dataset from the 500 °C experiments (Fig. 7B)  
343 yielded an equilibrium isotopic fractionation factor of  $\alpha_{\text{Fe}_4\text{N-NH}_3} = 0.9936$ , and a kinetic isotope  
344 fractionation factor of  $\alpha_{\text{N}_2\text{-Fe}_4\text{N}} = 0.9811$ .

345 To verify the equilibrium isotope fractionation factor between Fe<sub>4</sub>N and NH<sub>3</sub> at 500 °C, we  
346 examined the experiments with minor amounts of N<sub>2</sub> production, i.e., the experiments with  
347 durations up to 3.5 hours, in which the effect of N<sub>2</sub> production is not significant and the  $f_R$  and

348  $\delta_{RO}$  values can be corrected from the produced  $N_2$ . Such a modeling (using Equation 5 with the  
349 corrected  $f_R$  and  $\delta_{RO}$  values) yielded an  $\alpha_{Fe_4N-NH_3}$  value of  $0.9936 \pm 0.0004$  (Fig. 8B) at 500 °C.  
350 Incorporation of longer-duration experimental data in this modeling would result in significant  
351 decrease in the  $R^2$  value of the linear fitting and consequently large shift of the  $\alpha$  value. For this  
352 reason, the estimate of equilibrium isotope fractionation factor at 700 °C is not feasible because  
353  $N_2$  recovered from any of the experiments is more than half of the total N (Table 1; Fig. 1C). The  
354 experimental data at 700 °C are also too few to allow for an empirical modeling for the  
355 equilibrium and kinetic isotope fractionation factors using Equations (9)-(16).

356 With the  $1000\ln\alpha_{Fe_4N-NH_3}$  values determined here, and the  $1000\ln\alpha_{NH_4+-NH_3}$  and  $1000\ln\alpha_{N_2-}$   
357  $NH_3$  values from Li et al. (2021), we can further obtain  $1000\ln\alpha_{Fe_4N-N_2} = -15.7\text{‰}$  and  $1000\ln\alpha_{Fe_4N-}$   
358  $NH_4+ = -22.5\text{‰}$  at 300 °C and  $1000\ln\alpha_{Fe_4N-N_2} = -10.2\text{‰}$  and  $1000\ln\alpha_{Fe_4N-NH_4+} = -14.9\text{‰}$  at 500 °C.

359 These yielded N isotope fractionation factors are self-consistent with the characteristic  
360 temperature dependence of equilibrium isotope fractionation with greater magnitude at lower  
361 temperature and lesser magnitude at higher temperature. In contrast, kinetic N isotopic effect  
362 diminishes quickly with the increase in temperature (Deng et al., 2018) and shows no obvious  
363 temperature dependence in the high-temperature reactions of  $NH_3 \rightarrow N_2$  (Li et al., 2009). Our  
364 estimates are also consistent with theoretical predictions (Schauble et al., 2004) and experimental  
365 observations (Li et al., 2016; Dalou et al., 2019), which indicate that, at isotope equilibration, Fe-  
366 nitride is more  $^{15}N$ -depleted than other N species (e.g.,  $NH_4^+$ ,  $NH_3$ ,  $N_2$ ) in the lithosphere.

#### 367 **4.2.3. Kinetic isotope fractionation during decomposition of $Fe_4N$**

368 As discussed above,  $Fe_4N$  decomposition to  $N_2$  is considered to be unidirectional and the  
369 rate-limiting step of the entire process in our experiments. This is likely attributed to the strong N

370  $\equiv\text{N}$  bond of  $\text{N}_2$  that makes isotopic exchange between  $\text{N}_2$  and other N species difficult (Li et al.,  
371 2009). Li et al. (2014) suggested that a kinetic isotope effect would be expected for most of the  
372 reactions involving  $\text{N}_2$  in either reactant or product at relatively low pressures, which has already  
373 been observed in thermal decomposition of  $\text{NH}_3$  without catalyst (Li et al., 2009) and abiotic  
374 synthesis of N-bearing compounds from  $\text{N}_2$  (Kuga et al., 2014; Li et al., 2014). Accordingly, a  
375 kinetic isotope fractionation is also expected to be expressed in the produced  $\text{N}_2$  in our  
376 experiments. Consistently, all the produced  $\text{N}_2$  are more depleted in  $^{15}\text{N}$  than the initial  $\text{NH}_3$ ,  
377 which is in the opposite direction of the  $^{15}\text{N}$  enrichment order between  $\text{NH}_3$  and  $\text{N}_2$  at  
378 thermodynamic equilibrium (Li et al., 2021). The  $\delta^{15}\text{N}$  values of the produced  $\text{N}_2$  show an  
379 exponential increase pattern with the proceeding of  $\text{Fe}_4\text{N}$  decomposition (Fig. 2B), a typical  
380 feature of kinetic isotope fractionation that contrasts to the linear increase pattern of equilibrium  
381 isotope fractionation.

382 Through the sophisticated modeling of the 500 °C experimental data above (Fig. 7B), a  
383 kinetic N isotope fractionation factor of 0.9811 has been obtained for the  $\text{Fe}_4\text{N}$  decomposition  
384 reaction. To further verify this modeling result, a more straightforward Rayleigh fractionation  
385 model using Equation 7 was carried out. In this modeling, the “initial  $\text{Fe}_4\text{N}$ ” reservoir in each  
386 experiment did not have identical quantity and initial isotope composition but had variable  
387 values depending on the extent of  $\text{NH}_3$  decomposition. The quantity and  $\delta^{15}\text{N}$  value of the  
388 “initial  $\text{Fe}_4\text{N}$ ” from each experiment can be obtained by mass balance calculations from the  
389 quantities and isotope compositions of the recovered  $\text{Fe}_4\text{N}$  and  $\text{N}_2$  products. Using such a  
390 method, the modeling using Equation 7 with f value as low as 0.01 (Fig. 9) gave an  $\alpha_{\text{N}_2\text{-Fe}_4\text{N}}$   
391 value of  $0.9811 \pm 0.0009$  at 500 °C and  $0.9839 \pm 0.0011$  at 700 °C, which can also be expressed  
392 as isotopic enrichment factor  $\epsilon_{\text{N}_2\text{-Fe}_4\text{N}}$  of  $-18.9 \pm 0.9\text{‰}$  at 500°C and  $-16.1 \pm 1.1\text{‰}$  at 700 °C,

393 respectively. These values interestingly fall into the range (i.e.,  $\epsilon_{\text{N}_2\text{-NH}_3} = -19.2\text{‰}$  to  $-15.3\text{‰}$  at  
394  $600 - 800\text{ °C}$ ; Li et al., 2009) of the kinetic N isotope fractionations associated with the  
395 decomposition of  $\text{NH}_3$  to  $\text{N}_2$  without occurrence of Fe.

### 396 **4.3. Applications to roaldite tracer in meteorite**

397 In previous studies, nitride minerals have been considered to be able to record the isotopic  
398 signature of the material from which they were formed (e.g. Meibom et al., 2007; Harries et al.,  
399 2015; Grewal et al., 2021). Given the large range in  $^{15}\text{N}/^{14}\text{N}$  ratios ( $2-7 \times 10^{-3}$ , corresponding to a  
400 range of  $1500\text{‰}$ ; e.g. Meibom et al., 2007; Marty et al., 2011; Cartigny and Marty, 2013 for  
401 review), isotopic effects associated with formation and destabilization of nitrides have not been  
402 seriously considered in previous studies.

403 Our experimental results demonstrate that the formation of roaldite is fast and the produced  
404 roaldite is metastable at medium temperatures. The roaldite formation reaction can probably be  
405 extended to much lower temperatures. For example, Han et al. (2008) successfully observed  
406  $\text{Fe}_4\text{N}$  at temperatures  $< 300\text{ °C}$  by reacting  $\text{NH}_3$  using amorphous Fe. Although ammonia is not a  
407 significant component in the solar nebula, it can be in the atmosphere of ice bodies such as  
408 comets and more importantly in the atmosphere of giant planets. It is worth noting that, the  $\text{NH}_3$   
409 pressure required for  $\text{Fe}_4\text{N}$  formation is not high, e.g., Ertl et al. (1979) suggested that an  $\text{NH}_3$   
410 pressure as low as  $4 \times 10^{-7}$  bar could support the formation of  $\text{Fe}_4\text{N}$  at room temperature, despite  
411 that the reaction rate may be very slow in low- $\text{NH}_3$  pressure, low-temperature conditions. Even  
412 lower  $\text{NH}_3$  pressure is required with increase in temperature. Such a low  $\text{NH}_3$  pressure can be  
413 easily satisfied (Harries et al., 2015). The isotopic effects associated with  $\text{Fe}_4\text{N}$  formation is  
414 relatively small. As a result, the isotopic signature of the source N can be recorded in  $\text{Fe}_4\text{N}$ .

415 Our experimental results at 500 °C and 700 °C also verify previous suggestions that, under  
416 low pressures, Fe<sub>4</sub>N is unstable above 400 °C (van Voorthuysen et al., 2002). Interestingly, after  
417 most of the Fe<sub>4</sub>N being decomposed, a small amount of Fe<sub>4</sub>N survived and evolved into well  
418 crystalized shape in the long experiments (Figs. 5-6). The kinetic isotopic effect resulted in  
419 significant <sup>15</sup>N enrichment in the survived roaldite (Fig. 10). In extreme cases, the δ<sup>15</sup>N value of  
420 the remaining roaldite can be shifted from its original value for > 300‰, a magnitude that cannot  
421 be neglected even for meteorite studies. For example, the δ<sup>15</sup>N values (~50‰; Harries et al.,  
422 2015) of carlsbergite crystals (CrN) are very different from solar values (δ<sup>15</sup>N ~ -200‰, Marty et  
423 al., 2011; Meibom et al., 2007) but close to Earth's air (δ<sup>15</sup>N ~ 0‰) than most other N reservoirs  
424 in the early Solar System. Consequently, the carlsbergite crystals were considered to be derived  
425 from ices within regions of the protoplanetary disk that were affected by the distal wakes of  
426 shock waves (Harries et al., 2015). In another recent study, Grewal et al. (2021) found that the  
427 iron meteorites from non-carbonaceous reservoirs had a δ<sup>15</sup>N range from -96‰ to -1‰, whereas  
428 the iron meteorite from carbonaceous reservoirs had a δ<sup>15</sup>N range from 3‰ to 164‰. This  
429 difference was interpreted to reflect distinct nitrogen isotopic signature between their sources  
430 (Grewal et al., 2021). While we have no intention to argue against these interpretations, we point  
431 out that nitride denitridation could possibly lead to such large δ<sup>15</sup>N variations as well. Therefore,  
432 great caution should be taken to assess whether a nitride mineral has been partially decomposed  
433 before it can be used to infer source N signature.

434

## 435 **5. Conclusions**

436 To help understand the nitrogen isotope compositions of iron meteorites and nitride  
437 minerals in other meteorites, laboratory experiments were carried out to examine the nitridation  
438 and denitridation of metallic iron in an NH<sub>3</sub> atmosphere and associated nitrogen isotopic effects.  
439 The results show that Fe-nitrides, in particular, Fe<sub>4</sub>N, a chemical formula equivalent to roaldite  
440 mineral, can be formed in NH<sub>3</sub> atmosphere at a large temperature range from below 300 °C to  
441 700 °C. An equilibrium isotope fractionation between Fe<sub>4</sub>N and NH<sub>3</sub> is observed during the  
442 formation of Fe<sub>4</sub>N, with  $\alpha_{\text{Fe}_4\text{N-NH}_3} = 0.9907 (\pm 0.0004)$  at 300 °C and  $0.9936 (\pm 0.0004)$  at 500 °C,  
443 implying strong back reactions during Fe<sub>4</sub>N formation which have not been documented in  
444 relevant literature. At low-pressure conditions, Fe<sub>4</sub>N is stable at 300 °C but decomposes quickly  
445 into Fe and N<sub>2</sub> at temperatures  $\geq 500$  °C. Kinetic isotope fractionations with  $\alpha_{\text{N}_2\text{-Fe}_4\text{N}}$  values of  
446  $0.9811 (\pm 0.0009)$  and  $0.9839 (\pm 0.0011)$  were obtained for 500 °C and 700 °C, respectively.  
447 These observations suggest that roaldite (if not suffer denitridation by heat wave) can record the  
448 isotopic signature of its source nitrogen, but great caution is needed when using nitrogen isotope  
449 composition of roaldite mineral to trace source information because large isotopic shift up to  
450  $>300\text{‰}$  can be induced by partial decomposition of roaldite.

451

## 452 **Acknowledgements**

453 This study was partially funded by the CNRS “Programme National de Planétologie  
454 (PNP)” and NSERC Discovery grant. We thanks Drs. Eva Stüeken, Dennis Harries, and an  
455 anonymous reviewer for their constructive comments, and Associate Editor Yves Marrocchi for  
456 handling this paper.

457

458

459 **Reference**

- 460 Andersen, C.A., Keil, K., Mason, B. (1964) Silicon oxynitride: A meteoritic mineral. *Science* **146**, 256-  
461 257.
- 462 Bannister, F.A. (1941) Osbornite, meteoritic titanium nitride. *Mineral. Mag.* **26**, 36-44.
- 463 Buchwald, V.F. and Nielsen, H.P. (1981) Roaldite, a new nitride in iron meteorites. *Lunar Planet. Sci.*  
464 *XII*, 112-114.
- 465 Buchwald, V.F. and Scott, E.R.D. (1971) First nitride (CrN) in iron meteorites. *Nature Phys.Sci.* **233**,  
466 113-114.
- 467 Cartigny, P. and Marty, B. (2013) Nitrogen isotopes and mantle geodynamics: The emergence of life and  
468 the atmosphere–crust–mantle connection. *Elements* **9**, 359-366.
- 469 Coplen, T.B., Krouse, H.R., Böhlke, J.K. (1992) Reporting of nitrogen-isotope abundance. *Pure & Appl.*  
470 *Chem.* **64**, 907-908.
- 471 Dalou, C., Füri, E., Deligny, C., Piani, L., Caumon, M.-C., Laumonie, M. (2019) Redox control on  
472 nitrogen isotope fractionation during planetary core formation. *PNAS* **116**, 14485-14494.
- 473 Dauphas, N. (2017) The isotopic nature of the Earth's accreting material through time. *Nature* **541**, 521-  
474 524.
- 475 Deng, Y., Li, Y., Li, L. (2018) Experimental investigation of nitrogen isotopic effects associated with  
476 ammonia degassing at 0–70 °C. *Geochim. Cosmochim. Acta* **226**, 182-191.
- 477 Ertl, G., Nuber, M., Thiele, N. (1979) Formation and decomposition of nitrides on iron surface. *Z.*  
478 *Naturforsch.* **34**, 30-39.
- 479 Füri, E. and Marty, B. (2015) Nitrogen isotope variations in the Solar System. *Nature Geoscience* **8**, 515-  
480 522.
- 481 Grewal, D.S., Dasgupta, R. and Marty, B. (2021) A very early origin of isotopically distinct nitrogen in  
482 inner Solar System protoplanets. *Nature Astronomy*, Doi: 10.1038/s41550-020-01283-y.

483 Han, Y., Wang, H., Zhang, M., Su, M., Li, W.B., Tao, K. (2008) Low-temperature approach to synthesize  
484 iron nitride from amorphous iron. *Inorg. Chem.* **47**, 1261-1263.

485 Harries, D., Hoppe, P., Langenhorst, F. (2015) Reactive ammonia in the solar protoplanetary disk and the  
486 origin of Earth's nitrogen. *Nature Geosci.* **8**, 97-101.

487 Hayes, J.M. (2004) An Introduction to Isotopic Calculations Woods Hole Oceanographic Institution.

488 Inokuti, Y., Nishida, N., Ohashi, N. (1975) Formation of Fe<sub>3</sub>N, Fe<sub>4</sub>N and Fe<sub>6</sub>N<sub>2</sub> on the surface of iron.  
489 *Metallurg. Mater. Trans.* **6**, 773-784.

490 Javoy, M. (1998) The birth of Earth's atmosphere: the behaviour and fate of its major elements. *Chem.*  
491 *Geol.* **147**, 11-25.

492 Javoy, M., Kaminski, E., Guyot, F., Andraut, D., Sanloup, C., Moreira, M., Labrosse, S., Jambon, A.,  
493 Agrinier, P., Davaille, A., Jaupart, C. (2010) The chemical composition of the Earth: Enstatite  
494 chondrite models. *Earth Planet. Sci. Lett.* **293**, 259-268.

495 Keil, K. (1969) Titanium distribution in enstatite chondrites and achondrites, and its bearing on their  
496 origin. *Earth Planet. Sci. Lett.* **7**, 243-248.

497 Kiuchi, K. and McLellan, R.B. (1983) The solubility and diffusivity of hydrogen in well-annealed and  
498 deformed iron. *Acta Metall.* **31**, 961-984.

499 Kuga, M.C., N., Marty, B., Marrocchi, Y., Bernard, S., Rigaudier, T., Fleury, B., Tissandier, L. (2014)  
500 Nitrogen isotopic fractionation during abiotic synthesis of organic solid particles. *Earth Planet.*  
501 *Sci. Lett.* **393**, 2-13.

502 Leitner, J., Vollmer, C., Henkel, T., Ott, U. and Hoppe, P. (2018) An isotopic, elemental and structural  
503 study of silicon nitride from enstatite chondrites. *Geochim. Cosmochim. Acta* **235**, 153-172.

504 Li, L., Cartigny, P., Ader, M. (2009) Kinetic nitrogen isotope fractionation associated with thermal  
505 decomposition of NH<sub>3</sub>: Experimental results and potential applications to trace the origin of N<sub>2</sub> in  
506 natural gas and hydrothermal systems. *Geochim. Cosmochim. Acta* **73**, 6282-6297.

507 Li, L., Zheng, Y.-F., Cartigny, P., Li, J. (2014) Anomalous nitrogen isotopes in ultrahigh-pressure  
508 metamorphic rocks from the Sulu orogenic belt: Effect of abiotic nitrogen reduction during fluid–  
509 rock interaction. *Earth Planet. Sci. Lett.* **403**, 67-78.

510 Li, L., He, Y., Zhang, Z., Liu, Y. (2021) Nitrogen isotope fractionations among gaseous and aqueous  
511  $\text{NH}_4^+$ ,  $\text{NH}_3$ ,  $\text{N}_2$  and metal-ammine complexes: Theoretical calculations and applications.  
512 *Geochim. Cosmochim. Acta* **295**, 80-97.

513 Li, Y., Marty, B., Shcheka, S., Zimmermann, L., Keppler, H. (2016) Nitrogen isotope fractionation during  
514 terrestrial core-mantle separation. *Geochem. Perspect. Lett.* **2**, 138-147.

515 Marty, B., Chaussidon, M., Wiens, R.C., Jurewicz, A.J.G., Burnett, D.S. (2011) A  $^{15}\text{N}$ -poor isotopic  
516 composition for the Solar system as shown by Genesis Solar Wind samples. *Science* **332**, 1533-  
517 1536.

518 Marty, B. (2012) The origins and concentrations of water, carbon, nitrogen and noble gases on Earth.  
519 *Earth Planet. Sci. Lett.* **313-314**, 56-66.

520 Meibom, A., Krot, A.N., Robert, F., Mostefaoui, S., Russell, S.S., Petaev, M.I., Gounelle, M. (2007)  
521 Nitrogen and carbon isotopic composition of the Sun inferred from a high-temperature solar  
522 nebular condensate. *Astrophys. J.* **656**, L33-L36.

523 Pelka, R., Kielbasa, K., Arabczyk, W. (2014) Catalytic ammonia decomposition during nanocrystalline  
524 iron nitriding at 475 °C with  $\text{NH}_3/\text{H}_2$  Mixtures of different nitriding potentials. *J. Phys. Chem. C*  
525 **118**, 6178-6185.

526 Pelka, R., Moszyńska, I., Arabczyk, W. (2009) Catalytic ammonia decomposition over Fe/Fe<sub>4</sub>N. *Catal.*  
527 *Lett.* **128**, 72-76.

528 Piani, L., Marrocchi, Y., Rigaudier, T., Vacher, L.G., Thomassin, D., and Marty, B. (2020) Earth's water  
529 may have been inherited from material similar to enstatite chondrite meteorites. *Science* **369**,  
530 1110-1113.

531 Pizzarello, S., Feng, X., Epstein, S., Cronin, J.R. (1994) Isotopic analyses of nitrogenous compounds  
532 from the Murchison meteorite - ammonia, amines, amino-acids, and polar hydrocarbons.  
533 *Geochim. Cosmochim. Acta* **58**, 5579-5587.

534 Pizzarello, S., Williams, L.B., Lehman, J., Holland, G.P., Yarger, J.L. (2011) Abundant ammonia in  
535 primitive asteroids and the case for a possible exobiology. *PNAS* **108**, 4303-4306.

536 Poch, O., Istiqomah, I., Quirico, E., Beck, P., Schmitt, B., Theulé, P., Faure, A., Hily-Blant, P., Bonal, L.,  
537 Raponi, A., Ciarniello, M., Rousseau, B., Potin, S., Brissaud, O., Flandinet, L., Filacchione, G.,  
538 Pommerol, A., Thomas, N., Kappel, D., Mennella, V., Moroz, L., Vinogradoff, V., Arnold, G.,  
539 Erard, S., Bockelée-Morvan, D., Leyrat, C., Capaccioni, F., De Sanctis, M.C., Longobardo, A.,  
540 Mancarella, F., Palomba, E., Tosi, F. (2020) Ammonium salts are a reservoir of nitrogen on a  
541 cometary nucleus and possibly on some asteroids. *Science* **367**, eaaw7462.

542 Ponganis, K.V., Marti, K. (2007) Nitrogen components in IAB/III CD iron meteorites. *Meteorit. Planet.*  
543 *Sci.* **42**, 331-346.

544 Prombo, C.A., Clayton, R.N. (1993) Nitrogen isotopic compositions of iron meteorites. *Geochim.*  
545 *Cosmochim. Acta* **57**, 3749-3761.

546 Rubin, A.E., Choi, B.-G. (2009) Origin of halogens and nitrogen in enstatite chondrites. *Earth Moon*  
547 *Planets* **105**, 41-53.

548 Scott, K.M., Lu, X., Cavanaugh, C.M., Liu, J.S. (2004) Optimal methods for estimating kinetic isotope  
549 effects from different forms of the Rayleigh distillation equation. *Geochim. Cosmochim. Acta* **68**,  
550 433-442.

551 Schauble, E.A. (2004) Applying stable isotope fractionation theory to new systems. *Rev. Mineral.*  
552 *Geochem.* **55**, 65-111.

553 Sharygin, V.V., Ripp, G.S., Yakovlev, G.A., Seryotkin, Yu.V., Karmanov, N.S., Izbrodin, I.A.,  
554 Grokhovsky, V.I., Khromova, E.A. (2018) Uakitite VN, a new nitride in iron meteorites. 81st  
555 Annual Meeting of the Meteoritical Society, 22-27 July 2018 in Moscow, Russia. LPI  
556 Contribution No. 2067, 2018, id.6252

- 557 van Voorthuysen, E.H.D.M., Boerma, D.O., Chechenin, N.C. (2002) Low-temperature extension of the  
558 lehrer diagram and the iron-nitrogen phase diagram. *Metallurg. Mater. Trans.* **33**, 2593-2598.
- 559 Wriedt, H.A., Gokcen, n.A., Nafziger, R.H. (1987) The Fe-N (iron-nitrogen) system. *Bullet. Alloy Phase*  
560 *Diagram* **8**, 355-377.

